Trends in autoionization of Rydberg states converging to the 4*s* threshold in the Kr-Rb^+-Sr^{2+} isoelectonic sequence: Theory and experiment

A. Neogi, E. T. Kennedy, J.-P. Mosnier, P. van Kampen, and J. T. Costello*
National Centre for Plasma Science and Technology, School of Physical Sciences, Dublin City University, Glasnevin, Dublin 9, Ireland

G. O'Sullivan
Department of Experimental Physics, University College Dublin, Dublin 4, Ireland

M. W. D. Mansfield
Department of Physics, University College Cork, Cork, Ireland

Ph. V. Demekhin, B. M. Lagutin, and V. L. Sukhorukov†
Rostov State University of TC, 344038 Rostov-on-Don, Russia
(Received 24 October 2002; published 17 April 2003)

We have measured the photoabsorption spectra of the Kr-like ions Rb^+ and Sr^{2+} at photon energies corresponding to the excitation of $4s$-np resonances using, the dual laser plasma photoabsorption technique. Dramatic changes in the line profiles, with increasing ionization and also proceeding along the Rydberg series of each ion, are observed and explained by the trends in $4s$-transition amplitudes computed within a framework of configuration-interaction Pauli-Fock calculations. Total photoionization cross sections show very good agreement with relative absorption data extracted from the measured spectra.

DOI: 10.1103/PhysRevA.67.042707 PACS number(s): 32.80.Dz, 32.30.Jc

I. INTRODUCTION

Closed-shell atoms are prototypical systems for the detailed investigation of the atomic photoelectric effect. On the face of it, the spherically symmetric ground state should provide an ideal starting point for photoionization studies, yielding potentially simple excited electronic configuration states and concomitantly straightforward decay dynamics. Of course, in practice, the photoionization process is often mediated by strong electron correlation effects resulting in rather more subtle excitation and decay dynamics than a simple independent electron picture would suggest [1]. Although many systematic studies on photoionization of rare gas atoms exist [2] and a rather complete picture of the underlying physics has been established, there have been far fewer studies on their isoelectronic ions [3] resulting in a paucity of basic experimental and theoretical data. The difficulties inherent in the generation of sufficiently dense ion beams or absorbing columns of ions combined with intense and wavelength tunable light sources have been the main stumbling blocks to extensive and detailed experimentation on the ionic photoelectric effect.

So-called ''dual plasma'' experiments in which one plasma constitutes the absorbing column while the other acts as the vacuum-uv (vuv) continuum source have (to date) been the main sources of experimental data on photoabsorption or photoionization of ions. Early experiments with electrical discharge devices [4] gave way very rapidly to twin laser plasma based experiments [5] that have, in turn, undergone sustained development in the intervening 30 years [5–8]. After some pioneering experiments [9] in the mid-1980s, photoion spectroscopy based on merged ion and synchrotron radiation beams [10] looks set to become a major source of both relative and absolute cross-section data over the coming years. Table top two plasma experiments, which can access almost all atoms in all charge states, will act as pointers to interesting systems and continue to provide useful data in their own right. Further development of the very small number of experiments on photoelectron spectroscopy of ions [11], to date, will be key to unraveling the fine details of the excited state decay pathways, electronic structure of the product ion, angular distribution of the photoelectrons, etc. Of course, these latter experiments provide a severe experimental challenge and hence such ''complete'' experiments appear to be somewhat far into the future at present. They will certainly not achieve routine status until intense vuv or x ray free-electron lasers such as those under development at the Tesla Test Facility, DESY, Hamburg [12] and at SLAC in Stanford [13] become more widespread. It is also reasonable to expect symbiotic further development in standard models of atomic photoionization of ions [14].

Photoexcitation and photoionization are key processes in the universe. Quantitative data on photoexcitation and cross sections for photoionization are needed for the modeling of stellar atmospheres [15] and for the interpretation of many laboratory plasmas, particularly those designed to achieve ignition [16] and x ray laser action [17]. At photon energies extending into the vacuum ultraviolet and x ray regions, innershell and multielectron excitations are switched on. Interpretation of the associated multiple excitation and decay dynamics requires theoretical models that take into account the many-body nature of the problem. The challenge to experimentalists is to identify and measure the various competing processes involving well-described initial and final states and

*Electronic address: jtc@physics.dcu.ie
†Electronic address: vls@aaanet.ru

that for the theoreticians is to identify, isolate, and demonstrate the often-dominating role of electron-electron correlations. The importance of providing experimental data for the evaluation of atomic codes used to predict atomic and ionic properties is particularly important in view of large theoretical efforts represented in the projects such as OPACITY [18], IRON [19], and others. Furthermore, as atoms in molecular or condensed matter materials often exist in ionic form, the comparisons between the measurements on their free atom or ion counterparts and the corresponding species in the solid or molecular matrix can provide insight into the dominance or otherwise of the atomic versus matrix interactions. Experiments and calculations on positive ions provide opportunities to investigate the interplay between many-body electron-electron correlations and relativistic (spin orbit) effects by looking along either isonuclear or isoelectronic ionic sequences. For example, the evolution of wave function localization and configuration interaction with increasing ionization is often manifest in a quite dramatic redistribution of oscillator strength as seen in $4d$-subshell photoabsorption along the Ba-isonuclear sequence [20] and more recently along the Th-isonuclear sequence [21].

We studied experimentally and theoretically the evolution of $3s$-subshell photoabsorption at the beginning of the Ar isoelectronic sequence [22,23] for the species Ar, K^+, and Ca^{2+}. Dramatic changes in the profile parameter [24] q were observed ranging from q (sign) reversal to evolution from window resonances in Ar to almost symmetric absorption lines in Ca^{2+}. The observations were explained in Ref. [22] by showing the profiles to be highly sensitive to the relative positions of the $3s$-np resonances with respect to the ($3s$ and $3p$) Cooper minima [25] in each spectrum. In addition, the inclusion of doubly excited states had a very strong effect on the locations of the Cooper minima in the $3s$ and $3p$ photoionization cross sections and accordingly on the energies and profiles of $3s$-np resonances. In the paper of Lagutin *et al.* [23] a different approach was taken with cross sections computed using a configuration-interaction Pauli-Fock (CIPF) method. The results showed very good agreement with experiment and provided an explicit picture of the modulation of the $3s$-np resonance structure by the Cooper minimum as it moves through the $3s$ threshold with increasing ionization.

We extend this work here to the next row of the periodic table where the $4s$-subshell photoabsorption spectra of Kr-like Rb^+ and Sr^{2+} are presented for the first time. An integrated program of the CIPF calculations, which predate these recent measurements, provides a physical interpretation of the measured spectra and display excellent agreement with them. Apart from the intrinsic curiosity associated with studying the isoelectronic partners of one of the most investigated atoms in the periodic table (krypton), the sequence represents a test bed for teasing out the effect of increasing ionization on a high-Z closed shell atomic system. In addition, it provides an opportunity to identify the role played by the relativistic effects superimposed on the overarching electron correlation that determines the characteristic structure and dynamics of rare gas like ions.

This paper is organized as follows. In Sec. II we describe the experiment, in Sec. III we present the measured spectra, in Sec. IV we describe the theoretical methods underlying the photoionization calculations, in Sec. V we discuss in detail the evolution of photoionization for the first members of the Kr-like isoelectronic sequence, while in Sec. VI we reach some conclusions.

II. EXPERIMENT

The vuv spectra of rubidium and strontium ions were obtained, using the well-established dual laser plasma (DLP) technique [3,6–8]. In these experiments one laser plasma acts as an absorbing column of atoms or ions, while a second, synchronized tungsten or rare earth plasma is used to produce a pulsed continuum backlight stretching in wavelength from the uv (200 nm) right down to the soft-x-ray (2 nm) regions. DLP experiments are especially useful for obtaining the spectra of neutral to four times ionized elements [26]. A similar technique, termed point projection absorption spectroscopy (PPAS), has been used to obtain x-ray photoabsorption spectra particularly of more highly charged ions in the 0.1–2 nm spectra range [27]. We have recently shown that vuv and soft-x-ray DLP experiments with a time resolution of less than 100 ps are possible using this technique [21].

For the spectra presented here, a high power laser [Nd:YAG (YAG, yttrium aluminum garnet) fundamental, 700 mJ/15 ns pulse] was focused onto the target of interest via a spherocylindrical lens that generated a line plasma of height 100 ± 20 μm and length 9 ± 0.5 mm. Spectroscopically pure metal targets were used for the Sr plasmas. The surfaces were flat but roughened to reduce reflectivity. For the rubidium spectra we used compressed rubidium chloride crystal pellets which proved successful in our earlier measurements on $3d$-subshell spectra [28,29]. The front surface of each flat target could be displaced from the optic axis of the spectrometer by a known amount, using micrometer-controlled translation stages permitting different spatial regions of the plasma to be probed. After an adjustable time delay a second synchronized laser pulse (Nd:YAG laser of energy 850 mJ/pulse, 15 ns pulse width) was focussed tightly onto a different target (tungsten) giving rise to a second pointlike plasma that provided a vuv continuum source to backlight the absorbing plasma. The laser pulses were electro-optically synchronized by phase, locking the Pockels cells of each laser via a digital delay generator. The measured shot-shot jitter was better than 2 ns for all dual laser shots. The size of the vuv beam at the sample position was less than 300 μm in both the horizontal and vertical directions, which represents an upper limit on the spatial resolution achieved. Spectra were recorded photoelectrically with a McPherson 2.2 m grazing incidence vacuum spectrograph (slit width 20 μm, 1200 grooves/mm grating) fitted with an image intensified microchannel plate assembly, which was, in turn, fiber-optically coupled to a photodiode array detector [30]. There was no detectable radiation from the ''sample'' (absorbing) plasmas in the photon energy range of interest here. Hence we could simply measure the continuum in the absence (I_0) and presence (I) of the absorbing plasma and

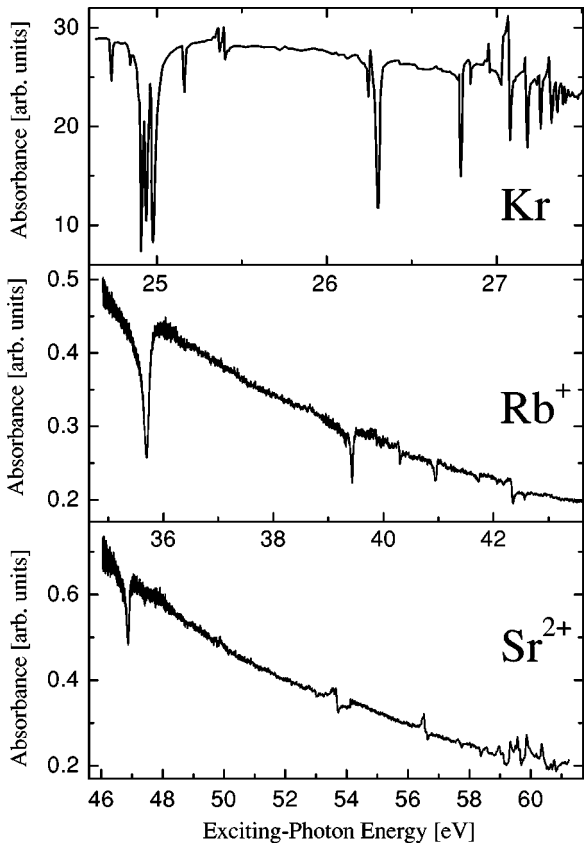

FIG. 1. Experimental photoabsorption spectra of Rb^+ and Sr^{2+} in the energy range from the $4s$-$5p$ Rydberg resonance up to $4s$-threshold (see Table II). The Kr data are taken from Ref. [31] for reference.

compute the absorbance $[\log_{10}(I_0/I)]$ directly. In the case where the absorbance lies below unity, opacity effects are quite small, the Beer-Lambert formula, $\log_{10}(I_0/I) = \sigma(\varepsilon)nL$, is applicable; hence the absorbance is directly proportional to the relative cross section. The spectral resolution was limited by the spatial resolution [$\sim$ five pixels full width at half maximum (FWHM)] of the channel electron multiplier array (CEMA) detector to approximately 35–55 meV over the (30–60 eV) photon energy range of interest here.

III. EXPERIMENTAL SPECTRA

We show in Fig. 1 the photoabsorption spectra of atomic Kr, Rb^+, and Sr^{2+} in the photon energy range where $4s^1 4p^6 np$ Rydberg and $4p^4 n'\ell' n''\ell''$ doubly excited resonances appear. The Kr data were not measured by us, but are taken from Codling and Madden [31]. The Rb^+ and Sr^{2+} spectra display well-developed resonance structure and required the accumulation of up to 400 laser shots to obtain the good signal-to-noise ratio shown. The on-target power density for both Rb and Sr plasmas was 5×10^9 W cm^{-2}. The spectra shown were recorded by firing the continuum pulse at delays of 200 ns and 50 ns after the initiation of the Rb and Sr sample plasmas, respectively. At these later times lowly charged ions, formed mainly by recombination become predominant. Also, the surfaces of the Rb and Sr targets were aligned exactly coincident with the vuv beam so that these plasmas were probed in regions very close to the focal zone. Under these conditions we found that one could record very pure spectra of Kr-like ions.

TABLE I. Measured profile parameters of $4s$-$5p$ resonances of Rb^+ and Sr^{2+}.

Profile parameter [33]	Rb^+	Sr^{2+}
E_0	35.71 ± 0.02	46.89 ± 0.03
Γ	0.09 ± 0.03	0.08 ± 0.03
q	0.24 ± 0.06	0.28 ± 0.07
ρ^2	0.40 ± 0.10	0.22 ± 0.05

It is immediately clear from Fig. 1 that all spectra are dominated by characteristic ''Fanolike'' [24] profiles which vary from window-type resonances with small q values of ~0.25 to asymmetric features with moderate values $|q| < 3$. The most striking difference between the Kr atom and the Rb/Sr ion spectra is the lowest energy resonance structure that consists of a single feature only for the ions. This is in stark contrast to the rather complex multiple structure observed in Kr around 25 eV, which is known to arise from strong the double excitations that overlay the main $4s$-$5p$ resonance [31,32]. On progressing up along the isonuclear sequence the complex doubly excited structure straddling the 25 eV photon energy range in Kr moves to higher energies in the ions, thereby simplifying the appearance of the low-energy portion of the ion spectra. We will develop this point later in the Sec. V.

We have fitted the usual Fano profile formula

$$\sigma = \sigma_0\left[1-\rho^2+\rho^2\frac{(q+\varepsilon)^2}{(1+\varepsilon^2)}\right], \tag{1}$$

where ρ is the overlap integral of the continuum states reached by direct and resonant ionization [33] and $\varepsilon=(E-E_0)/(\Gamma/2)$, where Γ is the resonance width and E_0 is the resonance energy position of the main $4s$-$5p$ resonances in the Rb^+ and Sr^{2+} spectra. The formula is applicable in these cases as these resonances are (unlike Kr) single and isolated features. The more highly excited features have, in the main, widths that lie below our resolution limit (better than 55 meV) and are also surrounded by the close-lying structure. The profile parameter values are shown in Table I. In the DLP experiments, we have previously observed that the profile widths and q-values of Fano-Beutler resonances depend on the absorbance, with optically thin spectra providing best values, subject to the effects of saturation and stray light [34]. Hence the profile widths and indices shown in Table I have been corrected, using the procedure described in Ref. [34]. The widths have had to be reduced by some 30%, while the q-values have been increased by $\sim10\%$. The error limits are arrived at by fitting a large number of the individual spectra that have been averaged to provide the traces shown in Fig. 1.

In a similar fashion to Ederer [35] we have added a background continuum term that decreases linearly with increasing photon energy to the Fano formula above.

IV. THEORY

Calculations of photoionization cross sections were performed in a manner similar to that described previously [36–38,32,23] and so only the essential details will be given here. Photoionization of the 4p- shell can be described by the following scheme:

$$\begin{array}{ccc} 4s^2 4p^6 + \gamma[0] & & 4p^5\varepsilon(s/d) \quad [\varepsilon] \\ & \Rightarrow & \updownarrow \\ & & \left\{ \begin{array}{c} \overline{4s^1 4p^6} np \\ 4s^2 4p^4 n(s/d) np \end{array} \right\} \quad [\mathrm{r}]. \end{array} \tag{2}$$

In this scheme the horizontal double arrow denotes the electric dipole interaction and the vertical double-ended arrow denotes the Coulomb interaction. Photoionization is manifested as an interference between the smooth direct ($2[\varepsilon]$) and resonance (2[r]) channels. The latter corresponds to the photoexcitation followed by the Auger decay of the $\overline{4s^1 4p^6} np$ Rydberg and $4s^2 4p^4 n(s/d) np$ doubly excited states. A summation over all states contained in the chain brackets was performed. The horizontal line above the $4s^1 4p^6$ configuration indicates that this state is strongly mixed with the set of $4s^2 4p^4 n(s/d)$ configurations. The amplitude ($2[\varepsilon]$) for the direct photoionization was computed according to the following scheme:

$$\begin{array}{ccc} 4s^2 4p^6 \ [0] & & 4p^5\varepsilon(s/d) \quad [\varepsilon] \\ \updownarrow & \Rightarrow & \updownarrow \\ 4p^4\{s/d\}\varepsilon(s/d) \ [a] & & 4s^1 4p^6\{p\} \quad [b] \\ \text{ISCI} & & \text{FISCI} \end{array} . \tag{3}$$

In this scheme the configurations that contribute to the transition amplitude due to both initial state configuration interaction (ISCI) and final state configuration interaction (FISCI) are shown. The letters in square brackets denote the states used in the description of the pathways and $\{\swarrow\}$ means a complete set of intermediate atomic orbitals (AOs) over which summation and integration are carried out. We note that here we do not take into account the transitions between the ''correcting'' configuration, i.e., pathways as $[0]\leftrightarrow[\mathrm{a}]\Rightarrow[\mathrm{b}]\leftrightarrow[\varepsilon]$ are neglected. Since we can neglect these pathways, notations such as $[0]\leftrightarrow[\mathrm{a}]\Rightarrow[\varepsilon]$ and $[0]\Rightarrow[\mathrm{b}]\leftrightarrow[\varepsilon]$ can be uniquely designated by labels (3[a]) and (3[b]), respectively. Therefore, the latter ones are used below. In scheme (3) the pathway (3[a]) describes the intrashell correlations, whereas the pathway (3[b]) corresponds to intershell correlations. In the present paper the transition amplitude (3) was computed within the RPAE approach [1] by applying the inverse matrix technique. It was then used in the pathways (4[e]) and (4[a]) of the following scheme describing the resonance amplitude (2[r]):

$$\begin{array}{ccc} 4s^2 4p^6 \ [0] & & \left(\begin{array}{c} \overline{4s^1 4p^6} \\ 4p^4 n(s/d) \end{array} \right) np[r] \\ \updownarrow & \Rightarrow & \updownarrow \\ \left\{ \begin{array}{c} 4s^1 4p^5\{s/d\} np \ [a] \\ 3d^9 4s^1\{p/f\} np \ [b] \\ 4p^4\{p/f\} np \ [c] \\ 4p^4 n(s/d)\{s/d\} \ [d] \end{array} \right\} & & \left\{ \begin{array}{c} 4p^5\{s/d\} \ [e] \\ 3d^9\{p/f\} \ [f] \end{array} \right\} \\ \text{ISCI} & & \text{FISCI} \end{array} . \tag{4}$$

The pathways (4[a]), (4[b]), (4[e]), and (4[f]) describe the intershell correlations while the pathways (4[c]) and (4[d]) contribute to the $[0]\Rightarrow[r]$ amplitude because of the presence of $4s^2 4p^4 n(s/d) np$ configurations in the final state. The scheme (4) was also used to compute the photoionization cross sections above $4s$-threshold. In this case to avoid the divergence problem in computing the pathway (4[d]) we applied the correlation function technique [37]. The schemes (2)–(4) give the general view of the problem while in the following sections we describe some of the salient features of computing the wave functions and the dynamical parameters entering these schemes.

A. Energy levels and wave functions for Kr-like ions

To calculate the eigenenergies and eigenfunctions of the initial and final states entering schemes (2)–(4) we used Pauli-Fock (PF) atomic orbitals (AOs). These AOs were computed by solving the PF equations that differ from their Hartree-Fock (HF) counterparts by the additional spherical terms describing mass velocity and Darwin corrections [39,40]. In effect, the PF approximation accounts for the relativistic compression of the atomic core without changing the HF configuration. Relativistic effects also contribute to the energies of atomic electrons, e.g., by increasing the ionization potential of $4s$-electron of Rb by 1.14 eV.

To obtain the wave functions for the resonance states $4s^1 4p^6 np$ and $4s^2 4p^4 n(s/d) np$ is a difficult computational problem due to the very large number of states that must be accounted for within intermediate coupling. To reduce this problem, we compute the wave functions of resonance states in two steps. At first we compute the ''core'' wave functions for the states $4s^1 4p^6$ and $4s^2 4p^4 n(s/d)$. In the second step we restrict the states included to those belonging to a number of low-lying configurations to which an np-electron is added.

To calculate the ''core'' wave function we used the configuration interaction technique. Within this approach a wave function having energy $\overline{E}$ and angular momentum $\overline{J}$ is represented as a linear combination of states having the true configuration K, orbital and spin momenta $\overline{LS}$, and other internal quantum numbers α of configuration K:

$$|\overline{EJ}\rangle = \sum_{K\alpha\overline{LSJ}} (K\alpha\overline{LSJ}|\overline{EJ})|K\alpha\overline{LSJ}\rangle. \tag{5}$$

TABLE II. Some parameters (in eV) used in the calculation of the "core" wave functions for Rb^+ and Sr^{2+}.

Quantity	Rb^+	Sr^{2+}
$\zeta_{4p}^{PF}(4p^4 4d)$[a]	**0.615**	**0.801**
$\zeta_{4p}^{expt}(4p^4 4d)$ [41]	**0.613**	**0.807**
$E^c(0)$	−35.66	−36.05
$E^{PF}(4p^5)$	26.56	42.21
$E^c(4p^5)$	1.10	1.24
$E^{theor}(4p^5)$	**27.66**	**43.45**
$E^{expt}(4p^5)$ [41]	**27.81**	**43.45**
$E^{PF}(4p^4)$	65.66	98.43
$E^c(4p^4)$	2.44	2.49
$E^{theor}(4p^4)$	**68.10**	**100.92**
$E^{expt}(4p^4)$ [41]	**68.01**	**100.98**
$\varkappa^{calc}(4p4p;4sn\not{\ell})$	1.43	1.44
$\varkappa^{fit}(4p4p;4sn\not{\ell})$	1.39	1.37
$E^{PF}(4s^1)$	46.92	65.19
$E^c(4s^1)$	0.48	0.42
$E_{DP}^c(4s^1)$	−3.77	−3.90
$E^{theor}(4s^1)=E^{expt}(4s^1)$ [41][b]	**43.63**	**61.71**

[a]The lines are highlighted to ease comparison between theory and experiment.

[b]Theoretical and experimental energies $E(4s^1)$ are equal (see text).

The numerical coefficients $(K\alpha\overline{LSJ}|\overline{EJ})$ are found by solving the secular equation. The configurations used in constructing the Hamiltonian matrix were the following: $4s^1 4p^6$, $4s^2 4p^4 ns(n=5-7,\varepsilon)$, and $4s^2 4p^4 nd$ $(n=4-8,\varepsilon)$. Continuum states covering the interval $\varepsilon=0.001-100$ Ry were included in a quasidiscrete manner [37,38]. These basis states result in secular equations of order 40, 57, 54, 30, 12 for $\overline{J}=1/2,3/2,5/2,7/2,9/2$, respectively. The states with $\overline{J}=7/2,9/2$ do not contribute the photoionization cross sections described by scheme (2) and were calculated only for the comparison between the theoretical and experimental [41] data for the "core" levels.

The diagonal matrix elements $\langle K\alpha\overline{LSJ}|\hat{H}|K\alpha\overline{LSJ}\rangle$ of the secular equation representing the energies of the basis state $|K\alpha\overline{LSJ}\rangle$ are computed relative to the center of gravity, $E(K)$, of the configuration K as

$$E(K\alpha\overline{LSJ})=\langle K\alpha\overline{LSJ}|\hat{H}|K\alpha\overline{LSJ}\rangle=E(K)+E^M(K\alpha\overline{LSJ}), \tag{6}$$

where the $E^M(K\alpha\overline{LSJ})$ is the multiplet correction including the Coulomb and $4p$-spin-orbital interactions. The parameters of the spin-orbital interaction ζ_{4p} computed for the $4p^4 4d$ configuration are compared with the experimental data in the compilation [41] in Table II, where one can see good agreement between computed and measured values of $\zeta_{4p}^{PF}(4p^4 4d)$. The center-of-gravity energies, $E(K)$, were calculated as a sum of PF $E^{PF}(K)$ and correlational, $E^c(K)$, total energies computed relative to the energies $E^{PF}(0)$ and $E^c(0)$, respectively, of the lowest Kr-like configuration $4s^2 4p^6$ as

$$E(K)=E^{PF}(K)+E^c(K). \tag{7}$$

To compute the correlational energies $E^c(K)$ we used, similar to Ref. [36], the second order of perturbation theory (PT) accounting for the interaction of configuration K with the set of all possible excited configurations differing from K by no more than two electrons. The virtual electron states used for the construction of the excited configurations contained *s*-, *p*-, *d*-, *f*-, *g*-, and *h*- channels each of which included the discrete AOs having a mean radius less or equal to 20 a.u. and continuum AOs with energies from 0.001 Ry to 1500 Ry. With the aim of checking the accuracy achieved, using the second order of PT in computing the center of gravity of the basis states, we calculated the total and partial energies entering equation (7) for the $4p^5$ and $4p^4$ configurations, which have only a few levels. The computed values as well as the reference energies $E^c(0)$ are listed in Table II for Rb^+ and Sr^{2+}. In the same table we show the corresponding experimental energies that were obtained by statistical averaging of the data given in the compilation of Moore [41]. One can recognize from this table that many-electron correlations contribute to the relative energies of the $4p^5$ and $4p^4$ configurations, the value of about 2 eV bringing the computed data into a good agreement with the measured ones.

The nondiagonal matrix elements entering the secular equation as well as the $E^M(K\alpha\overline{LSJ})$ entering equation (6) must be correspondingly corrected for the influence of the large number of high-lying states [36]. Having calculated the respective corrections to the Coulomb matrix elements within the second order of perturbation theory, the resulting reduction of the Coulomb matrix elements was expressed by scaling the original matrix elements downwards with appropriate factors. In constructing the Hamiltonian matrix we decreased the $4p4p$-$4sn\not{\ell}$ Coulomb interaction characterizing the interaction of the $4s^1 4p^6$ and $4s^2 4p^4 n(s/d)$ configurations by the factors $\varkappa^{fit}(4p4p;4sn\not{\ell})$ listed in Table II. Those parameters were chosen to align the computed and measured energies of the $4s^1 4p^6$ configurations and differ only slightly (see Table II) from the values $\varkappa^{calc}(4p4p;4sn\not{\ell})$ computed, as described in Ref. [36]. The $4p$-$4p$ and $4p$-$n\not{\ell}$ Coulomb interactions entering the Hamiltonian were scaled downwards by the factors of 1.20 and 1.12, respectively, and were taken to be the same as for the Kr atom [38].

The computed energies $E^c(K)$ and $E(K)$ for $4s^1 4p^6$ and some $4s^2 4p^4 n(s/d)$ configurations listed in Table III were used in the calculation of the wave functions (5). The computed eigenenergies are compared with the available experimental data [41] in Table IV for some levels. In this table we also show the weight of that basis state that has been used in

TABLE III. Many-electron corrections and energies for some configurations and ionization potentials of the np-Rydberg electron for Rb^+ and Sr^{2+} (see text).

				Rb^+				
K	$E^c(K)$	$E(K)$	$\Delta IP_{5p}(K)$	$IP_{5p}(K)$	$\Delta IP_{6p}(K)$	$IP_{6p}(K)$	$\Delta IP_{7p}(K)$	$IP_{7p}(K)$
$4s^14p^6$	0.48	47.40	0.45	7.94	0.19	4.09	0.11	2.53
$4p^45s$	1.51	49.64	0.67	9.22	0.17	4.31	0.10	2.62
$4p^46s$	2.12	58.72	0.65	10.64	0.23	4.97	0.09	2.79
$4p^44d$	1.57	49.67	0.64	8.36	0.21	4.18	0.09	2.54
$4p^45d$	2.11	58.98	0.67	10.37	0.24	4.70	0.07	2.70
$4p^46d$	2.28	62.52	0.56	11.71	0.20	5.41	0.07	2.98
				Sr^{2+}				
$4s^14p^6$	0.42	65.61	0.69	15.07	0.29	8.12	0.16	5.11
$4p^45s$	1.39	72.89	0.79	16.56	0.27	8.41	0.14	5.24
$4p^46s$	2.07	86.00	0.90	18.23	0.34	9.31	0.13	5.49
$4p^44d$	1.49	69.86	0.77	15.35	0.28	8.16	0.17	5.15
$4p^45d$	2.01	85.39	0.83	17.63	0.32	8.81	0.14	5.38
$4p^46d$	2.21	91.30	0.76	19.28	0.32	9.70	0.14	5.73

Ref. [41] for the assignment and the differences between the computed and measured level energies.

One can see from Table IV that the weight of the basis states used in Ref. [41] for the level identification is fairly small for some levels. Therefore, it could be meaningful to reassign some levels. For instance, in Rb^+ the eigenvectors $|48.18,1/2\rangle$ and $|48.78,1/2\rangle$ have the following largest weights:

$$|48.18,1/2\rangle = \underline{29\%(^3P)5s^4P_{1/2}} + 31\%(^3P)4d^4P_{1/2} + \cdots,$$

$$|48.78,1/2\rangle = 52\%(^3P)5s^4P_{1/2} + \underline{44\%(^3P)4d^4P_{1/2}} + \cdots,$$

where the underlined states are used for the level assignment [41]. One can see that the ''reverse'' assignment of these levels slightly increases the weight of the assigned states. However, we decided not to reassign the levels due to insufficient accuracy of our calculation estimated as a standard deviation between measured [41] and computed energies to be (in energy scale) 0.34 eV and 0.91 eV for Rb^+ and Sr^{2+}, respectively.

The additional nuclear charge in the sequence Kr-Rb^+-Sr^{2+} causes a change in the relative position of the basis configurations forming the Hamiltonian matrix. This has two important consequences.

(1) First, there is a decrease in the strength of the interaction between $4s^14p^6$ and $4s^24p^4n(s/d)$ configurations which can be seen from the trend in the spectroscopic factors for the $4s^14p^6\,^2S_{1/2}$ level along the Kr-Rb^+-Sr^{2+} sequence. The values are 0.64 [37], 0.72, 0.75 (Table IV). This behavior is caused by the rise in the energy of the $4s^24p^4n(s/d)^2S_{1/2}$ levels relative to the $4s^14p^6\,^2S_{1/2}$ level, since the electron density of the $4s^24p^4n(s/d)$ configurations is delocalized relative to that of the $4s^14p^6$ configuration.

(2) The second consequence of the increasing nuclear charge is the rise in energy of the levels connected with the $4s^24p^4ns$ configurations relative to the levels connected with the $4s^24p^4(n-1)d$ configurations. One can see this from Table IV where the position of the $4s^24p^45s$ and $4s^24p^44d$ levels is shown. This behavior is connected with the fact that the mean radius for the $5s$ AO (for $Rb^+\langle r_{5s} = 3.61$ a.u.$\rangle$) is larger than the mean radius for the $4d$ AO (for $Rb^+\langle r_{4d} = 2.53$ a.u.$\rangle$). The rise in energy of the levels connected with the $4s^24p^45s$ ''core'' configuration induces, in turn, an energy upshift in the corresponding doubly excited states connected with the $4s^24p^45s5p$ configuration. As a consequence, the well-pronounced resonances connected with $4s^24p^45s5p$ states in Kr, which straddle the $4s^14p^65p$ Rydberg resonance [32,31], are shifted towards the high-lying $4s^14p^6np$ Rydberg states in Rb^+ and Sr^{2+}. Therefore, the first $4s^14p^65p$ Rydberg resonance in Rb^+ and Sr^{2+} is observed as a single prominent resonance (see Fig. 1) whose shape can be used as a crucial test for the cross-section calculation.

B. Calculation of partial and total photoionization cross sections

The computed eigenvectors $|\overline{EJ}\rangle$ (5) for the core states with $J=1/2,3/2,5/2$ were used in computing the wave functions for the doubly excited states by simply adding the Rydberg electron to the state $|\overline{EJ}\rangle$. This procedure allows us to use only those core levels that contribute the structure between the $4p$ and $4s$ thresholds reducing therefore the order of the secular equation for the doubly excited states considerably. The numerical coefficients $(\overline{EJ}npjJ|EJ)$ entering the wave functions for the doubly excited states $|EJ(J=1)\rangle$,

$$|EJ\rangle = \sum_{K\alpha\overline{LS}J} (\overline{EJ}npjJ|EJ)|\overline{EJ}npjJ\rangle \qquad (8)$$

TABLE IV. Calculated and measured [41] energies (in eV) for some ionic limits of Rb^+ and Sr^{2+}.

Rb^+				Sr^{2+}			
Assignment [41]	E^{expt} [41]	E^{theor} Present	$E^{theor}-E^{expt}$	Assignment [41]	E^{expt} [41]	E^{theor} Present	$E^{theor}-E^{expt}$
72% $4s^14p^6\ ^2S_{1/2}$	43.63	43.63	0.00	75% $4s^14p^6\ ^2S_{1/2}$	61.71	61.71	0.00
95% $(^3P)4d\ ^4D_{7/2}$		46.51		94% $(^3P)4d\ ^4D_{7/2}$		65.86	
93% $(^3P)4d\ ^4D_{5/2}$		46.56		93% $(^3P)4d\ ^4D_{5/2}$		65.92	
92% $(^3P)4d\ ^4D_{3/2}$	46.40	46.66	0.26	91% $(^3P)4d\ ^4D_{3/2}$	65.78	66.05	0.27
93% $(^3P)4d\ ^4D_{1/2}$	46.65	46.76	0.11	91% $(^3P)4d\ ^4D_{1/2}$	66.12	66.19	0.07
89% $(^3P)5s\ ^4P_{5/2}$		47.64		95% $(^3P)4d\ ^4P_{1/2}$	68.99	68.21	−0.78
53% $(^3P)5s\ ^4P_{3/2}$	47.90	47.96	0.06	55% $(^3P)4d\ ^4P_{3/2}$	69.03	68.24	−0.79
29% $(^3P)5s\ ^4P_{1/2}$	48.35	48.18	0.17	85% $(^3P)4d\ ^4P_{5/2}$		68.64	
44% $(^3P)4d\ ^4P_{1/2}$	48.64	48.78	−0.14	26% $(^3P)4d\ ^2D_{3/2}$	69.63	68.42	−1.21
27% $(^3P)4d\ ^4P_{3/2}$	48.69	48.66	−0.03	24% $(^3P)4d\ ^2D_{5/2}$		69.04	
80% $(^3P)4d\ ^4P_{5/2}$		48.88					
				42% $(^3P)4d\ ^2P_{1/2}$		67.77	
52% $(^3P)5s\ ^2P_{3/2}$	48.84	48.48	−0.36	20% $(^3P)4d\ ^2P_{3/2}$	70.20	68.71	−1.49
92% $(^3P)5s\ ^2P_{1/2}$	49.25	49.15	−0.10				
				91% $(^3P)5s\ ^4P_{5/2}$		71.07	
20% $(^3P)4d\ ^2D_{3/2}$	49.01	48.60	−0.41	55% $(^3P)5s\ ^4P_{3/2}$	70.47	71.53	1.06
25% $(^3P)4d\ ^2D_{5/2}$		49.04		65% $(^3P)5s\ ^4P_{1/2}$	71.05	72.04	0.99
26% $(^3P)4d\ ^2P_{1/2}$		48.09		53% $(^3P)5s\ ^2P_{3/2}$	71.93	72.24	0.31
18% $(^3P)4d\ ^2P_{3/2}$	49.46	49.03	−0.43	95% $(^3P)5s\ ^2P_{1/2}$	72.58	72.76	0.18

were found by diagonalizing the resulting Hamiltonian matrix of order 170. The center-of-gravity energies $E(\overline{EJ}np)$ entering the Hamiltonian matrix were computed by using the ionization potentials of np electron, $\mathcal{V}_{np}(K)$, as

$$E(\overline{EJ}np)=\overline{E}-\mathcal{V}_{np}(K).$$

The $\mathcal{V}_{np}(K)$ values were calculated (taking into account many-electron correlations) with the aid of the following formula:

$$\mathcal{V}_{np}(K)=\mathcal{V}_{np}^{PF}(K)+\Delta\mathcal{V}_{np}(K)=[E^{PF}(K)-E^{PF}(K+np)]+[E^{c}(K)-E^{c}(K+np)].$$

In Table III we listed the correlational corrections $\Delta\mathcal{V}_{np}(K)$ and the resulting ionization potentials $\mathcal{V}_{np}(K)$ for the most important electron configurations of Rb^+ and Sr^{2+}.

The eigenvectors (8) were used in computing the resonant amplitudes $\langle EJ|\mathbf{D}|0\rangle$ for the scheme (4). In computing these amplitudes the Coulomb interaction entering scheme (4) was scaled downwards by a factor of 1.26 (for both Rb^+ and Sr^{2+}), found to be the optimum reduction in a previous study on Kr [37]. The same factor was used in computing direct amplitudes $\langle 4p_j^5\varepsilon\not{j}'J|\mathbf{D}|0\rangle$ in accordance with scheme (3). The transition amplitudes entering the equation for the photoionization cross section are

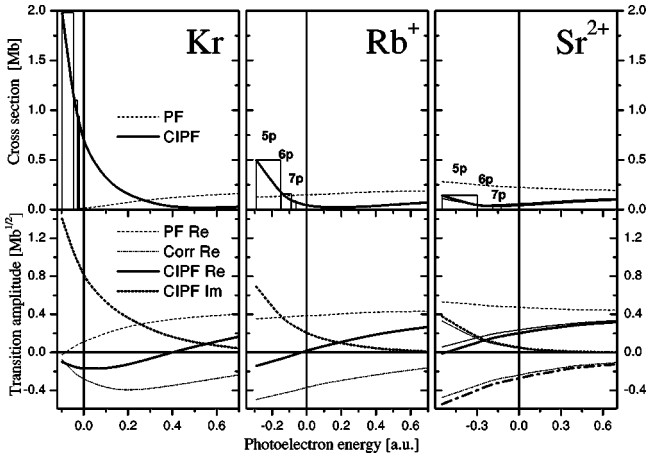

FIG. 2. Cross sections $\sigma_{4s}(\omega)$ (10) computed within the Pauli-Fock (PF) approach and also within the configuration-interaction PF approximation accounting for many-electron correlation. Lower panels show partial amplitudes for the $4s$-$(n/\varepsilon)p$ transition: PF Re, PF amplitude; Corr Re, real part of correlational amplitude (4[a]–[f]); CIPF Im, imaginary part of correlational amplitude (4[e],[f]), which coincides with the imaginary part of the total amplitude; CIPF Re, real part of the total amplitude. In the case of Sr^{2+} thin and thick lines represent calculation with the scaling factor equal to 1.26 and 1.05, respectively (see text).

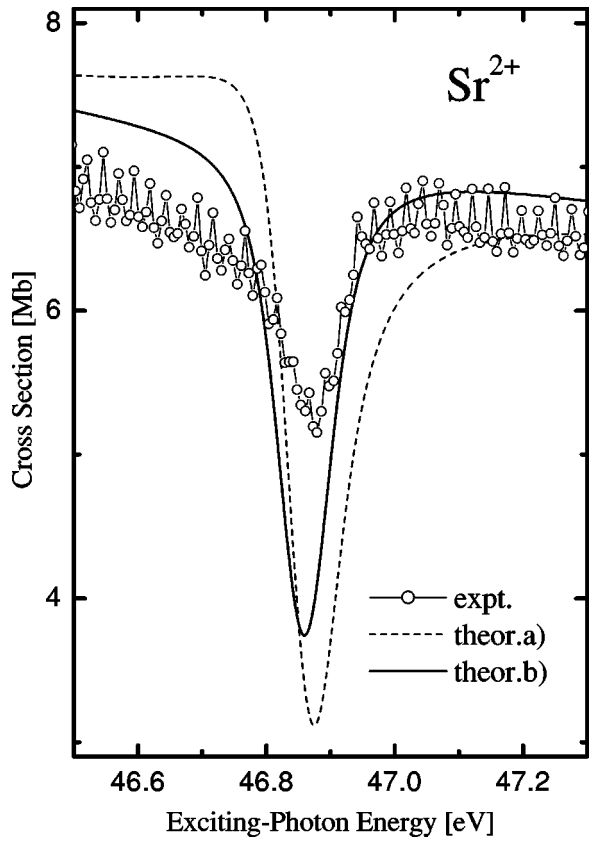

FIG. 3. Calculated and measured $4s$-$5p$ resonance in Sr^{2+}. Calculation with the scaling factor of 1.26 and 1.05, (a) and (b), respectively. Computed spectra are convoluted with the Gaussian function of FWHM $\Gamma = 55$ meV to simulate the experimental broadening.

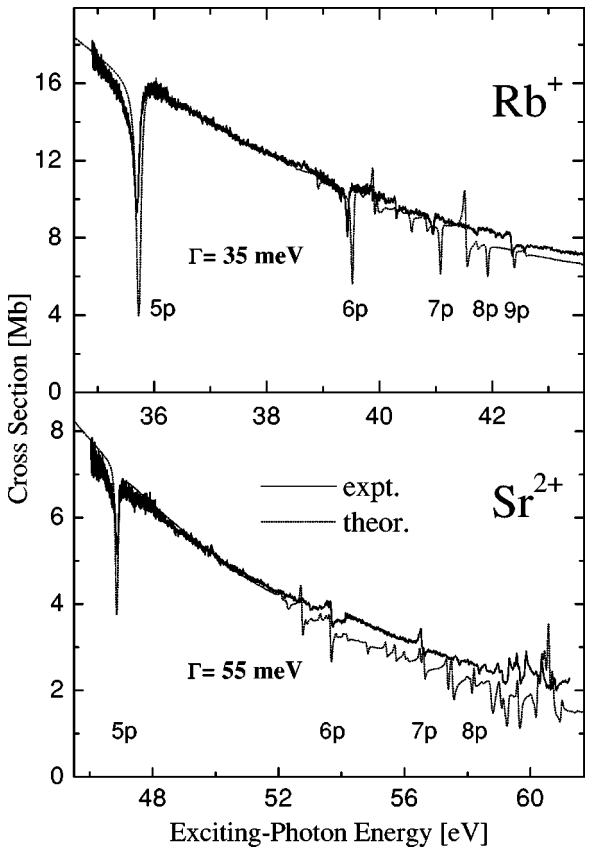

FIG. 4. Calculated and measured $4p$-photoabsorption spectra of Rb^+ and Sr^{2+}. The computed spectra are convoluted with a Gaussian profile of FWHM Γ shown in each panel. The positions of some computed Rydberg np resonances are marked.

$$\sigma_{4p}(\omega) = \frac{4}{3}\pi^2 \alpha a_0^2 \omega \sum_{\ell j j'} |\langle 4p_j^5 \varepsilon \ell j' J|\mathbf{D}|0\rangle + \sum_{EJ} \frac{\langle 4p_j^5 \varepsilon \ell j' J|\mathbf{H^{ee}}|EJ\rangle\langle EJ|\mathbf{D}|0\rangle}{(\varepsilon + E(4p^5) - E) + i\Gamma(EJ)/2}^2. \quad (9)$$

The bold letters for the Coulomb $\mathbf{H}^{ee}$ and transition, $\mathbf{D}$, operators show that the respective matrix elements were computed taking into account taken of many-electron effects; α, a_0, and ω are the fine-structure constant, Bohr radius, and exciting photon energy, respectively. Equation (9) represents the simplified solution of the ''many-resonance, many-continuum'' problem [24]. Strictly this problem should be solved by applying cumbersome techniques based either on real [42] or complex [43] numbers. However, in the case where the resonances do not overlap strongly, Eq. (9) results only in small differences in cross sections in comparison with that computed *via* the exact solution [28].

V. RESULTS AND DISCUSSION

In order to elucidate the general trends in the behavior of Rydberg resonances, we computed the ''smooth'' part of $4s$ partial photoionization cross section corresponding to scheme (4) by substituting εp waves for np orbitals:

$$\sigma_{4s}(\omega) = \frac{4}{3}\pi^2 \alpha a_0^2 \omega \sum_j |\langle \overline{4s^1 4p^6} \varepsilon p j J|\mathbf{D}|0\rangle|^2. \quad (10)$$

The computed $\sigma_{4s}(\omega)$ are shown in Fig. 2. In a manner described earlier [23] we present in the same figure the oscillator strength for the transitions into the Rydberg states as a smooth continuation of the continuum cross sections. The real and imaginary parts of the transition amplitude $\langle \overline{4s^1 4p^6}(n/\varepsilon) p j J|\mathbf{D}|0\rangle$ are also shown in Fig. 2 because the ratio

$$q = -\frac{\mathrm{Re}\langle \overline{4s^1 4p^6} n p j J|\mathbf{D}|0\rangle}{\mathrm{Im}\langle \overline{4s^1 4p^6} n p j J|\mathbf{D}|0\rangle}$$

is known to characterize the resonance profile. The transition amplitudes are normalized for convenience as

$$\sigma_{4s}(\omega) = \mathrm{Re}^2\langle \overline{4s^1 4p^6} n p j J|\mathbf{D}|0\rangle + \mathrm{Im}^2\langle \overline{4s^1 4p^6} n p j J|\mathbf{D}|0\rangle.$$

The value $\mathrm{Im}\langle \overline{4s^1 4p^6} n p j J|\mathbf{D}|0\rangle$ is determined to a very large extent by the pathway (4[e]), while $\mathrm{Re}\langle \overline{4s^1 4p^6} n p j J|\mathbf{D}|0\rangle$ is the result of destructive interference between the direct $[0] \Rightarrow [r]$ PF amplitude and all path-

ways (4[a]-[f]). Therefore, the direct and correlational parts [i.e., all the pathways (4[a]-[f])] of $\mathrm{Re}\langle \overline{4s^1 4p^6} npjJ|\mathbf{D}|0\rangle$ are also shown in Fig. 2.

One can recognize from Fig. 2 that the interference between direct and correlational amplitudes results in a minimum in the $\sigma_{4s}(\omega)$ cross section above the $4s$ threshold at about 0.4 a.u. in Kr, shifted toward the $4s$ threshold in Rb^+ and lying below the threshold in Sr^{2+}. The real part of the transition amplitude changes sign on passing through the high-lying Rydberg states in Rb^+. As a result, the sign of the q parameter will be reversed in that region. To observe this behavior for the high-lying Rydberg resonances could be quite difficult because these resonances are strongly blended with doubly excited states (see the above discussion concerning the "energy upshift" of the doubly excited states connected with the $4s^2 4p^4 5s$ configuration). In Sr^{2+} the real part of the amplitude is fairly small for the first $\overline{4s^1 4p^6} 5p$ resonance. Therefore, the measured shape of this resonance allows one to see more or less directly the interrelation between direct and correlational parts of the transition amplitude.

In the case of the $\overline{4s^1 4p^6} 5p$ resonance of Sr^{2+}, we decided to make further estimates of the factor used to scale downward the Coulomb interaction in computing the correlational amplitude (4[a]-[f]). The procedure showed that the scaling factor of 1.26 found to be optimum for the Kr calculation [37] and used in computing the cross sections for Rb^+ and Sr^{2+} is slightly overestimated for the positively charged ions. Therefore, we computed $\sigma_{4s}(\omega)$ (10) with a newly optimized scaling factor equal to 1.05. One can see from Fig. 2 that the change of both real and imaginary parts of the correlational component of the transition amplitude does not look considerable. But due to the destructive interference between direct and correlational amplitudes the resulting amplitude changed drastically. As a consequence, the computed shape of the $\overline{4s^1 4p^6} 5p$ resonance is also changed. One can see this clearly from Fig. 3, where the results of the computation of $\sigma_{4p}(\omega)$ with scaling factors equal to 1.26 and 1.05 are compared.

The cross sections $\sigma_{4p}(\omega)$ computed in accordance with Eq. (9) are presented in Fig. 4. To ease comparison between the theory and the experiment, the computed spectra were convoluted with a Gaussian instrumental profile having FWHM $\Gamma = 35$ and 55 meV for Rb^+ and Sr^{2+}, respectively. Measured cross sections were normalized using the computed ones in the smooth region between the $5p$ and $6p$ resonances. The slope of measured and computed cross sections were found to be very similar after the normalization procedure. The following points should be noted.

(1) The $5p$- and $6p$-Rydberg resonances in Rb^+ have the same sign of q parameter in both computed and measured spectra. This corresponds to Fig. 2, where the real part of transition amplitude crosses the abscissa axis in between $7p$ and $8p$ resonances. In Sr^{2+} this crossing point is shifted to lower exciting-photon energies. As a consequence, the sign of q parameter is changed beyond the $5p$ resonance, resulting in asymmetric resonances starting with the $4s$-$6p$ feature.

(2) The doubly excited states connected with $4s^2 4p^4 5s 5p$ states straddle the $6p$-Rydberg resonance region (and above it) blending with the high-lying $\overline{4s^1 4p^6} np$ Rydberg series. Interaction between $4s^2 4p^4 5s 5p$ and $\overline{4s^1 4p^6} np$ states can be as strong as indicated by the relative shift of the computed and measured high-lying resonances in Rb^+. The present calculation allow us to identify with certainty the first and second resonances while the precise identification of higher-lying resonances requires an improvement in the accuracy of calculation (see the above comparison for the energy positions of the core levels).

(3) Studying the Kr resonances [44] showed that the important additional information, useful for the interpretation of the experimentally observed features, can be obtained from the experiments where the angular distribution parameter for the photoelectrons $\beta^{el}(\omega)$ is measured. Studying the angular distribution of photoelectrons in our case could be even more enlightening because the ratio of the partial photoionization cross sections determining the $\beta^{el}(\omega)$ dependence is quite strongly modulated along the Kr-Rb^+-Sr^{2+} sequence. For instance, in the vicinity of the $\overline{4s^1 4p^6} 5p$ resonance the ratio $\sigma(4p^5 \varepsilon d)/\sigma(4p^5 \varepsilon s)$ decreases as 14/9/5 in Kr, Rb^+, and Sr^{2+}, respectively.

(4) With increasing ion charge, the oscillator strengths for the $\overline{4s^1 4p^6} np$ Rydberg series decrease as do the cross sections for direct photoionization (3). On the other hand, oscillator strengths for the doubly excited states depend only slightly on ion charge. As a consequence, the relative influence of the doubly excited states on the $\sigma_{4p}(\omega)$ increases along the row Kr-Rb^+-Sr^{2+}.

VI. CONCLUSION

We have measured the photoabsorption spectra of Rb^+ and Sr^{2+} in the vicinity of the $4s$-np resonances for the first time. The relative cross sections, extracted from the photoabsorption data, are well reproduced by the theoretical cross sections computed, using data from configuration-interaction Pauli Fock calculations. Rescaling the Coulomb interaction in channels (4[a]-[f]) is needed to better fit the $4s$-$5p$ resonance in Sr^{2+}, indicating a breakdown in the efficacy of second-order perturbation theory for this case. We observe that the complex doubly excited resonances straddling the first $4s$-$5p$ resonance in Kr moves to higher photon energy blending with $4s$-np resonances, where $n \geqslant 6$. This isolates the $4s$-$5p$ resonances in Rb^+ and Sr^{2+}, which can be parametrized by using a Fano formula. In addition, these resonances can now be an excellent probe for the study of intraatomic photoionization/photoexcitation dynamics for a Kr-like system. Studying the photoelectron angular distribution can provide additional information for the interpretation of the high-lying Rydberg resonances that are strongly mixed in Rb^+ and Sr^{2+} with the doubly excited states.

ACKNOWLEDGMENTS

This work was supported by the Higher Education Authority (HEA) Program for Research in Third Level Institutions (PRTLI) under the Irish Government's National Development Plan and by Enterprise-Ireland under the Basic Research Grants Scheme (RUS/1070409).

[1] M. Ya. Amusia, in *Atomic Photoeffect in Physics of Atoms and Molecules*, edited by K. T. Taylor (Plenum Press, New York, 1990).
[2] V. Schmidt, Rep. Prog. Phys. **55**, 1483 (1992).
[3] J.B. West, J. Phys. B **34**, R45 (2001).
[4] G. Mehlman-Balloffet and J.M. Esteva, Astrophys. J. **157**, 945 (1969).
[5] A. Carillon, P. Jaegle, and P. Dhez, Phys. Rev. Lett. **25**, 140 (1970).
[6] J.T. Costello, E.T. Kennedy, J.-P. Mosnier, P.K. Carroll, and G. O'Sullivan, Phys. Scr., T **34**, 77 (1991).
[7] E. Jannitti, P. Nicolosi, and G. Tondello, Phys. Scr. **41**, 458 (1990).
[8] P.K. Carroll and E.T. Kennedy, Phys. Rev. Lett. **38**, 1068 (1977).
[9] I.C. Lyon, B. Peart, J.B. West, and K. Dolder, J. Phys. B **19**, 4137 (1986).
[10] J.B. West, T. Andersen, R.L. Brooks, F. Folkmann, H. Kjeldsen, and H. Knudsen, Phys. Rev. A **63**, 052719 (2001).
[11] B. Rouvellou, J.M. Bizau, J. Obert, S. Al Moussalami, N. Berland, C. Blancard, E. Bouisset, D. Cubaynes, S. Diehl, L. Journel, J.C. Putaux, C. Vinsot, and F.J. Wuilleumier, Nucl. Instrum. Methods Phys. Res. B **134**, 287 (1998).
[12] J. Andruszkow *et al.*, Phys. Rev. Lett. **85**, 3825 (2000).
[13] A. Tremaine, X.J. Wang, M. Babzien, I. Ben-Zvi, M. Cornacchia, H.D. Nuhn, R. Malone, A. Murokh, C. Pellegrini, S. Reiche, J. Rosenzweig, and V. Yakimenko, Phys. Rev. Lett. **88**, 204801 (2002).
[14] I.D. Petrov, V.L. Sukhorukov, and H. Hotop, J. Phys. B **32**, 973 (1999).
[15] J.P. Aufdenberg, P.H. Hauschildt, S.N. Shore, and E. Baron, Astrophys. J. **498**, 837 (1998).
[16] J. Lindl, Phys. Plasmas **2**, 3933 (1995).
[17] H. Daido, Rep. Prog. Phys. **65**, 1513 (2002).
[18] C. Mendoza, Phys. Scr. T **65**, 198 (1996).
[19] C. Mendoza, Comput. Phys. Commun. **121**, 74 (1999).
[20] T.B. Lucatorto, T.J. McIlrath, J. Sugar, and S.M. Younger, Phys. Rev. Lett. **47**, 1124 (1981).
[21] O. Meighan, C. Danson, L. Dardis, C.L.S. Lewis, A. MacPhee, C. McGuinness, R. O'Rourke, W. Shaikh, I.C.E. Turcu, and J.T. Costello, J. Phys. B **33**, 1159 (2000).
[22] P. van Kampen, G. O'Sullivan, V.K. Ivanov, A.N. Ipatov, J.T. Costello, and E.T. Kennedy, Phys. Rev. Lett. **78**, 3082 (1997).
[23] B.M. Lagutin, Ph.V. Demekhin, I.D. Petrov, V.L. Sukhorukov, S. Lauer, H. Liebel, F. Vollweiler, H. Schmoranzer, O. Wilhelmi, G. Mentzel, and K.-H. Schartner, J. Phys. B **32**, 1795 (1999).
[24] U. Fano, Phys. Rev. **124**, 1866 (1961).
[25] J.W. Cooper, Phys. Rev. **128**, 681 (1962).
[26] H.S. Chakraborty, A. Gray, J.T. Costello, P.C. Deshmukh, G.N. Haque, E.T. Kennedy, S.T. Manson, and J.-P. Mosnier, Phys. Rev. Lett. **83**, 2151 (1999).
[27] D.M. O'Neill, C.L.S. Lewis, D. Neely, S.J. Davidson, S.J. Rose, and R.W. Lee, Phys. Rev. A **44**, 2641 (1991).
[28] A. Neogi, M. Martins, C. McGuinness, G. O'Sullivan, E.T. Kennedy, J.-P. Mosnier, P. van Kampen, and J.T. Costello, J. Phys. B **35**, 1329 (2002).
[29] A. Neogi, E.T. Kennedy, J.-P. Mosnier, P. van Kampen, J.T. Costello, C. McGuinness, and G. O'Sullivan, J. Phys. B **34**, L651 (2001).
[30] E.T. Kennedy, J.T. Costello, J.-P. Mosnier, A.A. Cafolla, M. Collins, L. Kiernan, U. Koble, M.H. Sayyad, M. Shaw M, B.F. Sonntag, and R. Barchewitz, Opt. Eng. **33**, 3984 (1994).
[31] K. Codling and R.P. Madden, J. Res. Natl. Bur. Stand., Sect. A **76**, 1 (1972).
[32] H. Schmoranzer, S. Lauer, F. Vollweiler, A. Ehresmann, V.L. Sukhorukov, B.M. Lagutin, I.D. Petrov, Ph.V. Demekhin, K.-H. Schartner, B. Magel, G. Mentzel, J. Phys. B **30**, 4463 (1997).
[33] U. Fano and J.W. Cooper, Phys. Rev. **137**, A1364 (1965).
[34] A. Gray, Ph. D. thesis, Dublin City University, 1999 (unpublished).
[35] D.L. Ederer, Phys. Rev. A **4**, 2264 (1971).
[36] B.M. Lagutin, I.D. Petrov, V.L. Sukhorukov, S.B. Whitfeld, B. Langer, J. Viefhaus, R. Wehlitz, N. Berrah, W. Mahler, and U. Becker, J. Phys. B **29**, 937 (1996).
[37] V.L. Sukhorukov, B.M. Lagutin, I.D. Petrov, H. Schmoranzer, A. Ehresmann, and K.-H. Schartner, J. Phys. B **27**, 241 (1994).
[38] B.M. Lagutin, V.L. Sukhorukov, I.D. Petrov, H. Schmoranzer, A. Ehresmann, and K.-H. Schartner, J. Phys. B **27**, 5521 (1994).
[39] R. Kau, I.D. Petrov, V.L. Sukhorukov, and H. Hotop, J. Phys. B **29**, 5673 (1996).
[40] R. Kau, I.D. Petrov, V.L. Sukhorukov, and H. Hotop, Z. Phys. D: At., Mol. Clusters **39**, 267 (1997).
[41] C.E. Moore, *Atomic Energy Levels*, Natl. Bur. Stand. (U.S.) Circ. No. 467 (U.S. GPO, Washington, D.C., 1971).
[42] F.H. Mies, Phys. Rev. **175**, 164 (1968).
[43] S.L. Sorensen, T. Åberg, J. Tulkki, E. Rachlew-Källne, G. Sundström, and M. Kirm, Phys. Rev. A **50**, 1218 (1994).
[44] M.G. Flemming, J.-Z. Wu, C.D. Caldwell, and M.O. Krause, Phys. Rev. A **44**, 1733 (1991).